Crystal Plasticity Analysis of Stress Partitioning Mechanisms and their Microstructural Dependence in Advanced Steels

Chao Pu,^a Yanfei Gao^{a,b}

Abstract

Two-phase advanced steels have an optimized combination of high yield strength and large elongation strain at failure, as a result of stress partitioning between a hard phase (martensite) and a ductile phase (ferrite or austenite). Provided with strong interfaces between the constituent phases, the failure in the brittle martensite phase will be delayed by the surrounding geometric constraints, while the rule of mixture will dictate a large strength of the composite. To this end, the microstructural design of these composites is imperative especially in terms of the stress partitioning mechanisms amongst the constituent phases. Based on the characteristic microstructures of dual-phase and multilayered steels, two polycrystalline aggregate models are constructed to simulate the microscopic lattice strain evolution of these materials during uniaxial tensile tests. By comparing the lattice strain evolution from crystal plasticity finite element simulations with advanced in situ diffraction measurements in literature, this study investigates the correlations between the material microstructure and the micromechanical interactions on the intergranular and interphase levels. It is found that although the applied stress will be ultimately accommodated by the hard phase and hard grain families, the sequence of the stress partitioning on grain and phase levels can be altered by microstructural designs. Implications of these findings on delaying localized failure are also discussed.

Keywords: dual phase steel; multilayered steel; lattice strain; crystal plasticity finite element method

1. Introduction

Demands from automotive and aerospace industries have stimulated the investigations of multi-phase steels that can achieve both high strength and high ductility and thus have tremendous applications in vehicle and aircraft body structures. In advanced high strength steels (AHSS) [1] that are broadly used in these applications, two phases are introduced, including a hard phase that provides high strength and the other phase that is capable of large elongation prior to failure. As a result of complex intergranular and interphase interactions, a good balance of strength and elongation strain can be achieved. One example is the dual phase (DP) steel, consisting of low carbon, hard martensite phase (about 5-30 vol. %) dispersed in the ferrite matrix [2–4]. An alternative design beyond AHSS is the multilayered steel as processed by rolling bonding of stacked, alternating martensite and austenite layers [1,5,6]. On the so-called "banana curves" plotting the tensile strength against fracture elongation (i.e., a ductility measure) in [1], DP steel shows a better combination of strength and ductility than conventional steels. However,

^a Department of Materials Science and Engineering, University of Tennessee, Knoxville, TN 37996

^b Materials Science and Technology Division, Oak Ridge National Laboratory, Oak Ridge, TN 37831

the multilayered steel has the potential to even outperform than the dual phase steel as shown in [1] and as reviewed in [6].

Provided with strong interfaces between the constituent phases, the failure strain in the brittle martensite phase will be delayed by the surrounding geometric constraints, while the rule of mixture will dictate a large strength of the composite. To this end, the microstructural design is imperative especially in terms of the stress partitioning mechanisms amongst the constituent phases. In recent works [4,5], advanced diffraction measurements were conducted on both types of multi-phase steels under tensile tests. Advanced diffraction measurements provide an in situ, nondestructive and deeppenetrating method to capture the evolution of grain-level and phase-level deformation behavior. Lattice strain evolution in DP 980 steel (68 vol. % ferrite and 32 vol. % martensite) was collected using high energy X-ray diffraction (HEXRD) [4]. Neutron diffraction measurements were conducted in [5] on multilayered steel with alternating martensitic and austenitic layers. The objective of these diffraction studies is to investigate the stress partitioning mechanism between the two constituent phases, but the direct information from these measurements, being the lattice strain evolution, has a complex convolution of intergranular and interphase interactions. Considering a singlephase polycrystal material, we can see that the hkl diffraction peaks will be governed by a number of grains whose $\{hkl\}$ planes satisfying the diffraction condition. The peak shift will give rise to the lattice strain, and microscopically this is a result of the lattice stretching of these {hkl} planes in the chosen grain family. Some grain families will yield before others, and the yield sequence is determined by the intergranular interaction. With the presence of two phases, the respective yield sequences of $\{hkl\}$ grain families in these two phases will be further complicated by the interphase interaction.

The understanding of the lattice strain evolution in these mutli-phase steels can be obtained by numerical simulations. For instance, an elasto-plastic model is adopted in [7] to investigate the macroscopic hardening behavior by using a modified Swift equation describing the stress-strain relationship. Such a model, however, does not have a direct reference to the inhomogeneous deformation fields on gain levels. On the other hand, lattice strains can be successfully investigated by microstructure-dependent analysis, such as the crystal plasticity finite element method (CPFEM) [8-10], and visco-plastic selfconsistent (VPSC) method [4,11,12] for both FCC and BCC materials. In the VPSC model, each grain is assumed to be embedded in a homogeneous matrix, of which the material properties obey the macroscopic deformation properties. The consistency condition is derived from the fundamental Eshelby solution that determines the deformation fields induced by the inclusion or inhomogeneity. Although efforts have been attempted to extend the VPSC model to multi-phase materials [4,12], important questions such as the interplay between intergranular and interphase deformation fields and the dependence of stress partitioning mechanisms on microstructural designs (i.e., dual phase as opposed to multilayers) cannot be clearly addressed. An explicit treatment of these material microstructures by CPFEM will be clearly more advantageous.

In this work, CPFEM simulations are conducted to investigate the stress partitioning amongst various grain families in both phases. A representative volume element (RVE)

approach is used to describe the unique microstructures in DP 980 steel, and a full-scale model for the multilayered steel. Geometric input parameters include volume fraction, characteristic grain shape, and phase distributions as derived from the scanning electron microscopy (SEM) image in [4] for DP 980 steel and from optical images in [5] for the multilayered steel. By fitting to all the available {hkl} lattice strains from experimental observations, the crystal plasticity parameters can be determined. Three deformation stages can be identified, each of which exhibits microstructure-dependent intergranular and interphase characteristics. Our simulations will allow us to explore possible microstructure and material designs that can be used to tune the stress partitioning, the study of which will help understand and possibly delay the localized failures in these materials.

2. Model description

An RVE model containing two phases is constructed for DP steel simulation in Fig. 1. The entire model is of $100\mu m \times 100\mu m \times 100\mu m$ in dimension, and is made of $10 \times 10 \times 10$ cubic units. Note that during the annealing process, the austenitic grains are nucleated randomly at the ferritic grain boundaries, and then they grow the fastest along the grain boundaries. After further cooling, prior austenitic grains are transformed into martensite, and this thermal treatment history determines the shape and locations of martensite phase. A numerical method simulating the above process is introduced in [13] and implemented to simulate the microstructural evolution in DP steel in [2]. Here a simplified model is used in our simulation that captures the essential microstructural features in DP steel. The cubic unit in Fig. 1(a) is composed of one martensitic grain and one ferritic grain, and the martensite phase is aligned along the grain boundaries, as shown in the cubic unit in Fig. 1(b). That is, it is placed randomly on one of the six surfaces of the cubic unit. A total of $3 \times 3 \times 3$ cubic elements (C3D8 – three dimensional 8-node continuum element in ABAQUS finite element software) are used to represent this martensite and austenite duo. As compared to the mesh in [13], the simplification lies on the use of cubic elements. Since lattice strains are based a statistical average of many grains, this simplification has been proved to be effective and computationally less intensive [8-10]. To satisfy the volume fraction of martensitic phase (Table 1), the martensitic phase has $3 \times 3 \times 1$ cubic elements. A two-dimensional view of the mesh in Fig. 1(b) exhibits similar phase patterns as in SEM images. These grains will be assigned with random crystallographic orientations. The faces of RVE model with normal directions of -x, -y and -z as shown in Fig. 1(a) are prescribed with the symmetric boundary conditions. A ramping displacement with a constant rate is applied on the surface with z normal direction. The diffraction vector is parallel with the loading direction that is the z direction in Fig. 1(a).

As described by the detailed manufacturing procedure in [5], the multilayered steel is manufactured by hot-rolling low-carbon martensitic steel layer and austenitic stainless steel layers. The full-scale model sketched in Fig. 2 simulates a three-layer sample, whereas the layer thickness and volume fraction are derived from optical observations in [5] (Table 2). From symmetric conditions, only one eighth of the full model is meshed in our simulations, leading to a body of $250\mu m \times 250\mu m \times 500\mu m$ containing $25 \times 25 \times 10^{-2}$

50 C3D8 cubic elements, where each cubic element represents one grain. According to the SEM image in [14] and transmission electron microscopy (TEM) image in [15], the average grain size of WT780C martensitic phase is about 11.1µm and that of SS316L austenitic phase is about $10\mu m$. Thus our simulations do not distinguish this slight difference in grain size. Again these grains and phases are assigned with random crystallographic orientations without considering the texture effect. As sketched in Fig. 2, the symmetric planes are applied with symmetric boundary conditions, while a ramping displacement is applied in parallel to the layer interface direction in the numerical model. The diffraction vector is also parallel with the loading direction.

The CPFEM simulation is based on the classic crystal plasticity theory in Peirce et al. [16], and the ABAQUS user defined subroutine (UMAT) by Huang [17]. The UMAT has been modified by Zheng et al. [18] in order to investigate the lattice strain evolution in a polycrystal aggregate. Here a concise review of the CPFEM is given below. For the Schmid-type crystal plasticity, the plastic deformation rate is regarded as a summation over all slip systems,

$$\dot{F}_{ik}^{p} F_{kj}^{p-1} = \sum_{\alpha=1}^{N_{slip}} \dot{\gamma}^{(\alpha)} s_i^{(\alpha)} m_j^{(\alpha)} \tag{1}$$

where N_{slip} denotes the total number all activated slip directions, $\dot{\gamma}^{(\alpha)}$ is the slip rate of the α -th slip system, $s_i^{(\alpha)}$ and $m_i^{(\alpha)}$ represent the slip direction and slip plane normal, and F_{kj}^p is the plastic deformation gradient. The slip rate updates according to the power-law flow rule,

$$\dot{\gamma}^{(\alpha)} = \dot{\gamma}_0 \left| \frac{\tau^{(\alpha)}}{\tau_{flow}^{(\alpha)}} \right|^n \operatorname{sgn}(\tau^{(\alpha)})$$
 (2)

where $\dot{\gamma}_0$ is the reference strain rate, $\tau^{(\alpha)}$ and $\tau^{(\alpha)}_{flow}$ are the resolved shear stress and current slip strength of the α -th slip system respectively, and n is the stress exponent. The hardening behavior of $au_{flow}^{(lpha)}$ is described by the Peirce-Asaro-Needleman model,

$$\dot{\tau}_{flow}^{(\alpha)} = \sum_{\beta} h_{\alpha\beta} |\dot{\gamma}^{(\beta)}| \tag{3}$$

where $h_{\alpha\beta}$ is the hardening moduli. The self-hardening modulus is expressed as,

$$h_{\alpha\alpha} = h(\gamma) = h_0 \operatorname{sech}^2 \left| \frac{h_0 \gamma}{\tau_s - \tau_0} \right|$$
 (4)

where no summation is assumed for the repeated index α , h_0 is the initial hardening modulus, τ_0 is the initial slip strength, and τ_s is the saturation slip strength. And the latent hardening part is given by

$$h_{\alpha\beta} = h(\gamma) [q + (1 - q)\delta_{\alpha\beta}]$$
 (5)

 $h_{\alpha\beta}=h(\gamma)\big[q+(1-q)\delta_{\alpha\beta}\big]$ where $\alpha\neq\beta$, and q is the latent hardening coefficient.

Among all the grains, we choose the ones whose $\{hkl\}$ planes satisfy the diffraction condition. That is, their <hkl> directions are parallel to the diffraction vector. In practice, we allow a small tolerance of $\pm 5^{\circ}$ between these two vectors in order to obtain sufficient fraction of grains. Then the lattice strain, ε_{hkl} , is evaluated by

$$\varepsilon_{hkl} = \frac{\sum_{N=1}^{N_{\text{grain}}} \int \varepsilon_{ij}^{\text{elastic}} q_i q_j d\Omega_N}{\sum_{N=1}^{N_{\text{grain}}} \int d\Omega_N}$$
 (6)

where N_{grain} denotes the number of grains whose direction is within $\pm 5^{\circ}$ with respect to diffraction vector, q_i is the component of diffraction vector, $\varepsilon_{ij}^{\text{elastic}}$ is the Lagrange-Green strain,

$$\varepsilon_{ij}^e = \frac{1}{2} \left(F_{ik}^e F_{kj}^e - \delta_{ij} \right) \tag{7}$$

and F_{ij}^e is the elastic deformation gradient.

3. Lattice strain evolution

Before presenting our simulation results, a mechanistic interpretation of the lattice strain is briefly given for a single-phase polycrystal. According to the work in [10], lattice strain partitioning, or splitting, in individual grain families indicate a sequence of yielding in these families. Consider a simple view in which every grain is subjected to the same strain as the macroscopic one, i.e., the Taylor iso-strain model. The first gain family to reach yield is the one that has the lowest yield strain, whereas the yield strain is inversely proportional to the product of Schmid factor and directional modulus. Assuming no hardening, the grain family upon yielding will not have further elastic deformation, so its lattice strain will remain constant with respect to the further increase of the applied stress. Correspondingly, a larger portion of the applied stress will be supported by the grain families that have not reached yield, and the lattice strains of these grain families will increase rapidly. The yield sequence, $\{hkl\}_1 \rightarrow \{hkl\}_2 \rightarrow \dots \rightarrow \{hkl\}_N$, will thus govern the lattice strain splitting on the lattice strain versus applied stress plots. This is denoted as intergranular interaction in this study. This simple view can be generalized to the twophase polycrystal, and we will see the interactions of two yield sequences, i.e., $\{hkl\}_1^{\text{phase I}} \rightarrow \{hkl\}_2^{\text{phase II}} \rightarrow \dots \rightarrow \{hkl\}_N^{\text{phase II}}$, and $\{hkl\}_1^{\text{phase II}} \rightarrow \{hkl\}_2^{\text{phase II}} \rightarrow \dots \rightarrow \{hkl\}_N^{\text{phase II}}$. These two sequences may be very likely intertwined; equivalently speaking, we may not be able to separate the intergranular and interphase interactions.

As described in introduction, HEXRD and neutron diffraction measurements were carried out to obtain the lattice strain evolution of different $\{hkl\}$ s for both phases in DP 980 steel and multilayered steel under uniaxial tensile test. These experimental data are given in discrete markers in Figs. 3 and 4, while our simulations are given in solid curves. The mechanistic understanding in the preceding paragraph will help us determine the CPFEM constitutive parameters (see Tables 3 and 4). The elastic constants, C_{11} , C_{12} and C_{44} , can be found in literature such as [4], and our simulations will further fine-tune these values so as to fit the initial lattice strains when all grains and phases are in elastic deformation. Note that the initial lattice strain splitting is primarily determined by the Schmid factor (which is governed by the choice of slip system) and the directional modulus (which is governed by the elastic anisotropy). The slip system is chosen as the $\{110\}<111>$ system for both ferrite and martensite phase, and as the $\{111\}<10>$ for austenite. The initial slip strength, τ_0 , can be estimated from the deviation of the lattice strain from linearity as the applied stress increases and exceeds the elastic stage, being about 700MPa in Fig. 3 and about 250MPa in Fig. 4. In single-phase polycrystals, τ_0 relates to the macroscopic yield

stress by the Taylor factor, being about 3.0 for non-textured FCC and BCC polycrystal. This is how we estimate τ_0 for the soft ferrite and austenite phases in Tables 3 and 4. However, the Taylor-factor approach cannot be applied to estimate the initial slip strength in martensite phase. When the martensite phase yields, some grain families in ferrite or austenite phases have already reached yield but some have not. Therefore the slip strength of the martensite phase is obtained by fitting to the experiments in [4] and [5]. Also the hardening parameters as specified in Eqs. (3)-(5) are obtained from fitting the entire lattice strain curves for all these phases.

3.1 Intergranular versus interphase interactions

Experiments and simulations are presented for DP 980 steel in Fig. 3. Because the ferrite and martensite phases have similar lattice structure and constants, the diffraction peaks are convoluted, and only the {200} peaks have been separated in [4]. Thus experimental data are only given for {200} lattice strains for the constituent phases. For the other lattice strains, our CPFEM results are compared to the VPSC model presented in [4]. Results for the austenite/martensite multilayered steel only compare CPFEM results to the neutron diffraction measurements in Fig. 4. VPSC model was not attempted because the unique microstructure in multilayered steel differs from typical polycrystalline aggregates.

The lattice strain evolution can be categorized into several stages. At low applied stresses, all grain families and phases deform elastically, and the initial slopes in this Stage 1 are governed by the elastic constants and microstructure. Note that the martensite phase is much harder than the other ferrite or austenite phase. Therefore, we denote a Stage 2 in which none of the grain families in martensite phase yields. In Fig. 3, this corresponds to the applied stress in the range of about 600 MPa to 1200 MPa, while in Fig. 4 in the range of about 250 MPa to 380 MPa. Since the martensite phase deforms elastically in Stage 2, the ratios of the various $\{hkl\}$ lattice strain slopes for this phase should remain roughly unchanged. The lattice strain curves for the soft phase in this stage, although all moving horizontally together, will branch in Fig. 3 and Fig. 4 because the applied stress is shifted among these grain families. With the further increase of the applied stress, some grain families in the martensite phase will yield, leading to the Stage 3. Because of the low applied stress in Fig. 3, Stage 3 is not observed, but our simulations in Fig. 5 suggest that eventually it will take place. In Stage 3, the start of the yield sequence in the martensite phase, $\{hkl\}_1^{\text{martensite}} \rightarrow \{hkl\}_2^{\text{martensite}} \rightarrow \dots \rightarrow \{hkl\}_N^{\text{martensite}}$, falls into the middle place of the yield sequence of the soft phase, $\{hkl\}_1^{\text{ferrite/austenite}} \rightarrow \{hkl\}_N^{\text{ferrite/austenite}}$. Additionally, the hardening rates of these two phases are different in this stage. Therefore, it is observed that the lattice strain slopes of martensite phase decrease while those of austenite phase increase in Stage 3 of Fig. 4.

In Fig. 4, some discrepancies are observed for martensitic {110} lattice strain between CPFEM simulations and experiments, as marked by the dashed ellipse. This is likely due to the simplified microstructure in Fig. 2, while the actual microstructure has a transition of grain sizes from the interface and there are some correlations of crystallographic

orientations in the grains adjacent to the interface. Also the actual grain shape in martensite phase is of lathe like.

3.2 Effectiveness of stress transfer amongst phases and grain families

Although both DP and multilayered steels have similar stress partitioning/transferring behavior, the multilayered steel is found to be much more superior in terms of the improved failure strain. Such a difference can be understood from the dependence of Stage 2 and Stage 3 on the composite microstructure. From a geometric point of view, the deformation field in the multilayered steel can be approximated by the iso-strain model, while that in the DP steel lies between the iso-strain and iso-stress models. That is, each grain or phase in DP steel is subjected to a complex constraint from the neighboring grains or phases, and the deformation field, although being close to the iso-strain model, can be nicely described by the self-consistent model. In the iso-strain case, the applied stress will be shift from the phase/grain with low yield strain to that with high yield strain, and such an "effectiveness" of stress transfer is more obvious than the iso-stress model or the self-consistent model. Previously in [5], an iso-strain assumption is introduced to evaluate the stress transfer behavior in these two types of different steels. However, in this simple model, the soft phase is assumed to not bear the applied stress after it yields. The work in [5] further compares the measurements in Fig. 3 and Fig. 4, which are clearly for different types of soft phase and different volume fraction. Moreover, the isostrain assumption neglects the intergranular interactions due to the inhomogeneous deformation fields. In contrast, here we present CPFEM simulations to quantitatively evaluate the effectiveness of stress transfer in these two types of composite microstructures.

To demonstrate that the effectiveness of stress transfer is higher in multilayered steel, we construct a fictitious DP model with martensite and austenite phases. As shown in Fig. 5(a), the cubic unit in this modified DP model consists of 22 vol. % martensite and 78 vol. % austenite, which is consistent with the volume fractions in the multilayered steel. The entire RVE model contains $10 \times 10 \times 10$ of such cubic units with randomly assigned crystallographic orientations for both phases. The {211} lattice strains are given for the martensite phase in the fictitious DP model and the multilayered steel in Fig. 5(b). The general features in the three stages remain the same, while the magnitude of the martensite lattice strain is significantly higher in the multilayered steel, implying that a larger portion of the applied stress will be transferred to the hard phase. For instance, at an applied stress of about 420 MPa, the increase of lattice strain from fictitious DP to multilayered model is about 0.15%, corresponding to an extra stress of about 200 MPa on this grain family. In spite of the improved the effectiveness of stress transfer in multilayered steel, the microstructure will unavoidably make the inelastic deformation anisotropic if loading in different directions. All the lattice strains in the work are reported for the loading direction, and it is anticipated that the lattice strains in the transverse directions will be lower for the martensite phase in multilayered steel than those for the DP model.

The stress partitioning analysis will shed lights on understanding the superior elongation strain in the multilayered steel. For the multilayered steel, it has been found in [6] that the failure is preceded by a local debonding between austenite and martensite layers, and a slight necking and then brittle fracture in the debonded martensite. Debonding arises from the strain mismatch in the two phases, as evidenced in the synchrotron x-ray experiments in a composite consisting similar hard and soft phases [19]. In the multilayered steel, because of the improved lattice strain on the martensite phase as shown in Fig. 5(b), the mismatch of total strain between neighboring phases is significantly reduced. As a consequence, the debonding and subsequent localized failure will be delayed, which help explain the improved macroscopic performance in such a material.

4. Summary

Intergranular and interphase interactions in DP steel and multilayered steel are investigated by crystal plasticity finite element simulations, with comparisons to the lattice strain measurements by advanced diffraction techniques in literature. Microstructural models are constructed from experimentally observed features such as the locations of martensite phase in DP steel. Three deformation stages are identified on the lattice strain evolution with respect to the applied stress. The yield sequences of various grain families in the two phases are found to be intertwined, leading to a complex interplay amongst the inhomogeneous deformation fields on grain and phase levels. The dependence of the effectiveness of stress transfer on the microstructure is investigated by the comparisons of a fictitious DP model (with austenite and martensite) and the multilayered steel. The enhanced stress transfer to the martensite phase will help delay localized failure such as martensite phase fracture and interface debonding.

Acknowledgements

This work was supported by the U.S. Department of Energy, Office of Science, Basic Energy Sciences, Materials Sciences and Engineering Division (YFG), and by a graduate fellowship from the Joint Institute for Neutron Sciences at the University of Tennessee (CP).

References

- [1] Barabash, R. I., Barabash, O. M., Ojima, M., Yu, Z., Inoue, J., Nambu, S., Koseki, T., Xu, R., and Feng, Z., 2013, "Interphase strain gradients in multilayered steel composite from microdiffraction," Metall. Mater. Trans. A, **45**(1), pp. 98–108.
- [2] Chen, P., Ghassemi-Armaki, H., Kumar, S., Bower, A., Bhat, S., and Sadagopan, S., 2014, "Microscale-calibrated modeling of the deformation response of dual-phase steels," Acta Mater., **65**, pp. 133–149.
- [3] Kim, D. H., Kim, S.-J., Kim, S.-H., Rollett, A. D., Oh, K. H., and Han, H. N., 2011, "Microtexture development during equibiaxial tensile deformation in monolithic and dual phase steels," Acta Mater., **59**(14), pp. 5462–5471.
- [4] Jia, N., Cong, Z. H., Sun, X., Cheng, S., Nie, Z. H., Ren, Y., Liaw, P. K., and Wang, Y. D., 2009, "An in situ high-energy X-ray diffraction study of micromechanical behavior of multiple phases in advanced high-strength steels," Acta Mater., **57**(13), pp. 3965–3977.
- [5] Ojima, M., Inoue, J., Nambu, S., Xu, P., Akita, K., Suzuki, H., and Koseki, T., 2012, "Stress partitioning behavior of multilayered steels during tensile deformation measured by in situ neutron diffraction," Scr. Mater., **66**(3-4), pp. 139–142.
- [6] Koseki, T., Inoue, J., and Nambu, S., 2014, "Development of multilayer steels for improved combinations of high strength and high ductility," Mater. Trans., **55**(2), pp. 227–237.
- [7] Ohashi, T., Roslan, L., Takahashi, K., Shimokawa, T., Tanaka, M., and Higashida, K., 2013, "A multiscale approach for the deformation mechanism in pearlite microstructure: Numerical evaluation of elasto-plastic deformation in fine lamellar structures," Mater. Sci. Eng. A, **588**, pp. 214–220.
- [8] Zheng, L. L., Gao, Y. F., Wang, Y. D., Stoica, a. D., An, K., and Wang, X. L., 2013, "Grain orientation dependence of lattice strains and intergranular damage rates in polycrystals under cyclic loading," Scr. Mater., **68**(5), pp. 265–268.
- [9] Zheng, L. L., Gao, Y. F., Lee, S. Y., Barabash, R. I., Lee, J. H., and Liaw, P. K., 2011, "Intergranular strain evolution near fatigue crack tips in polycrystalline metals," J. Mech. Phys. Solids, **59**(11), pp. 2307–2322.
- [10] Wong, S. L., and Dawson, P. R., 2010, "Influence of directional strength-to-stiffness on the elastic–plastic transition of fcc polycrystals under uniaxial tensile loading," Acta Mater., **58**(5), pp. 1658–1678.
- [11] Clausen, B., Lorentzen, T., and Leffers, T., 1998, "Self-consistent modelling of the plastic deformation of F.C.C. polycrystals and its implications for diffraction measurements of internal stresses," Acta Mater., **46**(9), pp. 3087-3098.
- [12] Jia, N., Lin Peng, R., Wang, Y. D., Johansson, S., and Liaw, P. K., 2008, "Micromechanical behavior and texture evolution of duplex stainless steel studied by neutron diffraction and self-consistent modeling," Acta Mater., **56**(4), pp. 782–793.
- [13] Saylor, D., Fridy, J., El-Dasher, B., Jung, K.-Y., and Rollett, A., 2004, "Statistically representative three-dimensional microstructures based on orthogonal observation sections," Metall. Mater. Trans. A, **35**(7), pp. 1969–1979.

- [14] Tanaka, Y., Kishimoto, S., Yin, F., Kobayshi, M., Tomimatsu, T., and Kagawa, K., 2009, "Multi-scale deformation behavior for multi-layer steel by in-situ FE-SEM," Fourth Int. Conf. Exp. Mech., **7522**, p. 7520N–1.
- [15] Feng, K., Cai, X., Li, Z., and Chu, P. K., 2012, "Improved corrosion resistance of stainless steel 316L by Ti ion implantation," Mater. Lett., **68**, pp. 450–452.
- [16] Peirce, D., Asaro, R. J., Needleman, A., and Park, A., 1983, "Overview: material rate dependence and localized deformation in crystalline solids," Acta Mater., **31**(12), pp. 1951–1976.
- [17] Huang, Y., 1991, "A user-material subroutine incorporating single crystal plasticity in the ABAQUS finite element program," Mechanics Report 179, Divion of Engineering and Applied Science, Harvard University.
- [18] Zheng, L., 2011, "Micromechanical studies of intergranular strain and lattice misorientation fields and comparisons to advanced diffraction measurements." PhD Thesis, University of Tennessee.
- [19] Barabash, R. I., Bei, H., Gao, Y. F., and Ice, G. E., 2011, "Interface strength in NiAl–Mo composites from 3-D X-ray microdiffraction," Scr. Mater., **64**(9), pp. 900–903.

| Material | Ferrite Phase (vol. %) | Martensite Phase (vol. %) |
|--------------|------------------------|---------------------------|
| DP 980 steel | 68 | 32 |

Table 1: The volume fractions of constituent phases in DP 980 steel.

| Material | Austenite layer thickness (mm) | Martensite layer thickness (mm) | Martensite Phase Volume fraction |
|--------------------|--------------------------------|---------------------------------|----------------------------------|
| Multilayered Steel | 0.4 | 0.2 | 20% |

Table 2: Parameters used in the three-layer model in Fig. 2 for the multilayered steel.

| Phase | <i>C</i> ₁₁ (GPa) | <i>C</i> ₁₂ (GPa) | <i>C</i> ₄₄ (GPa) | n | h_0 | $	au_0$ | $	au_{\scriptscriptstyle S}$ | q |
|------------|------------------------------|------------------------------|------------------------------|----|-------|---------|------------------------------|---|
| Ferrite | 237 | 141 | 116 | 10 | 800 | 200 | 800 | 1 |
| Martensite | 237 | 141 | 116 | 10 | 1000 | 550 | 1000 | 1 |

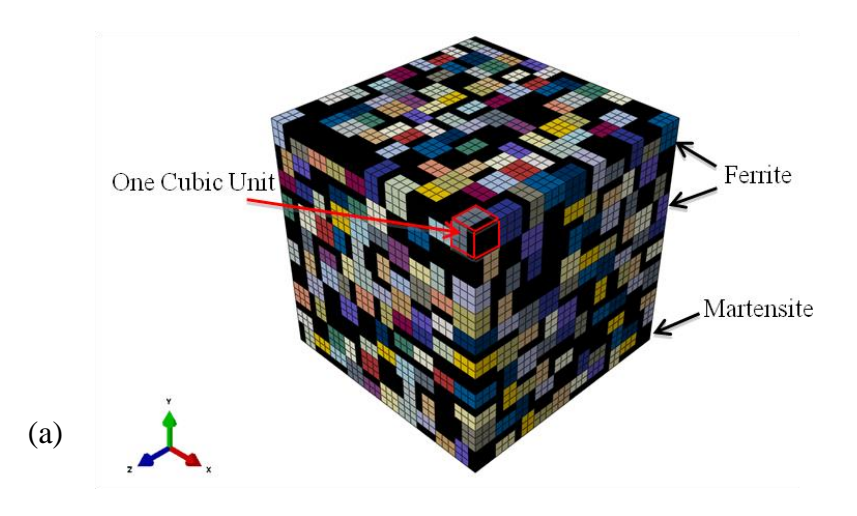
Table 3: CPFEM parameters for the DP 980 steel.

| Phase | C ₁₁ (GPa) | C ₁₂ (GPa) | C ₄₄ (GPa) | n | h | τ_0 | τ_{s} | q |
|------------|--------------------------|--------------------------|--------------------------|----|-----|----------|---------------------|---|
| Austenite | 204.6 | 137.7 | 126.2 | 10 | 400 | 65 | 180 | 1 |
| Martensite | 268 | 110 | 78 | 10 | 300 | 290 | 2000 | 1 |

Table 4: CPFEM parameters for the austenite/martensite multilayered steel.

Figure Captions

- Figure 1 (a) Representative volume element (RVE) for DP 980 steel. The RVE model size is $100\mu m \times 100\mu m \times 100\mu m$ consisting of $10 \times 10 \times 10$ cubic units. Black elements denote the martensitic phase, while colored elements correspond to ferritic grains. (b) Each cubic unit consists of $3 \times 3 \times 3$ C3D8 solid elements including one martensite grain and one ferritic grain. Due to the martensitic phase transformation during annealing, these martensitic phases are located at the grain boundaries. A two-dimensional cut of the RVE mesh is shown to compare with the SEM image in [4].
- Figure 2 Schematic illustration of CPFEM model of multilayered steel. One eighth of the model is meshed due to symmetric considerations.
- Figure 3 Crystal plasticity finite element simulations of lattice strain evolution in DP 980 steel (solid lines), as compared to experimental data (discrete markers [4]) and viscoplastic self-consistent simulations (dash curves).
- Figure 4 Lattice strain evolution in multilayered steel, with the comparisons of CPFEM simulations in this work and experimental data in [5]. A red dashed ellipse indicates the deviation of modeling from experimental data.
- Figure 5 (a) Schematic illustration of the cubic unit used in the fictitious DP material that consists of martensite and austenite phases. (b) Direct comparisons of {211} lattice strain evolution in the fictitious DP material and multilayered steel of martensite and austenite phases.



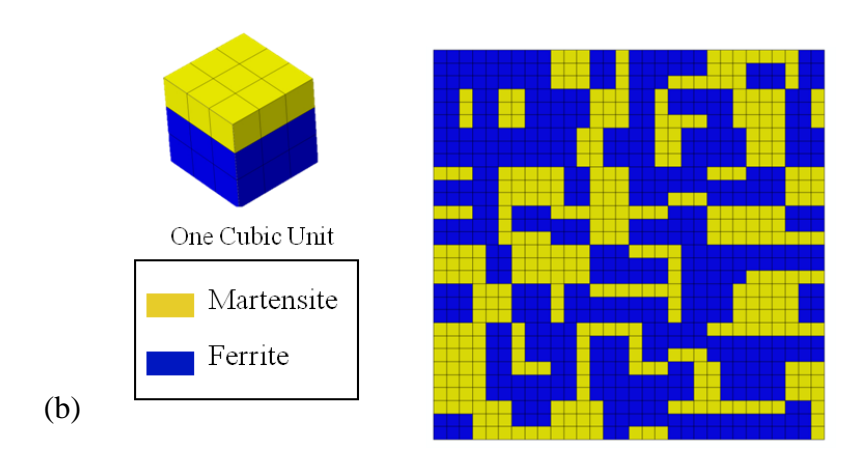
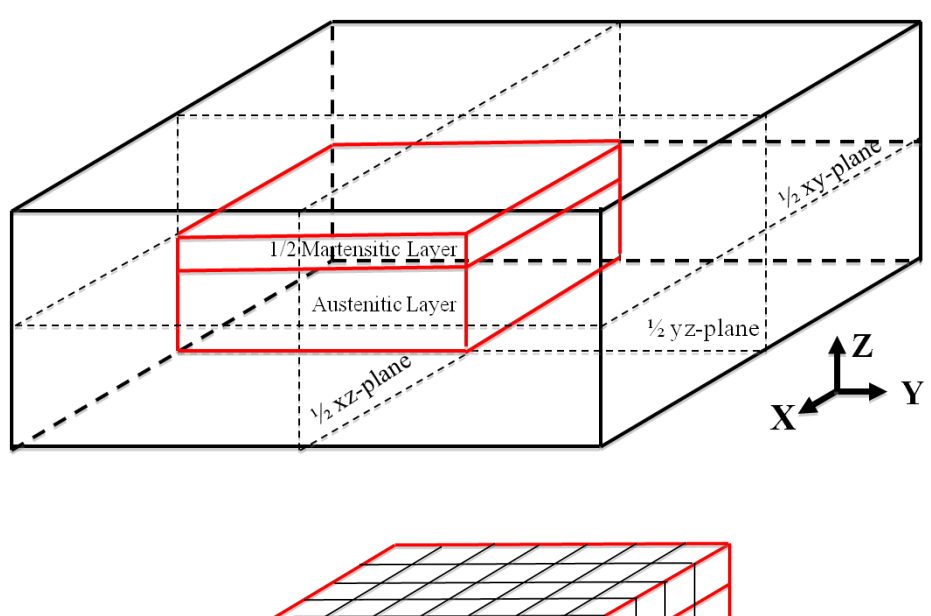


Figure 1



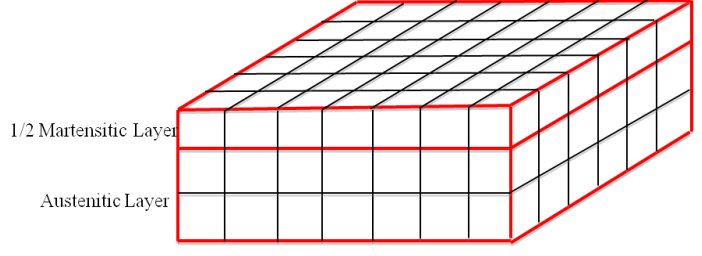


Figure 2

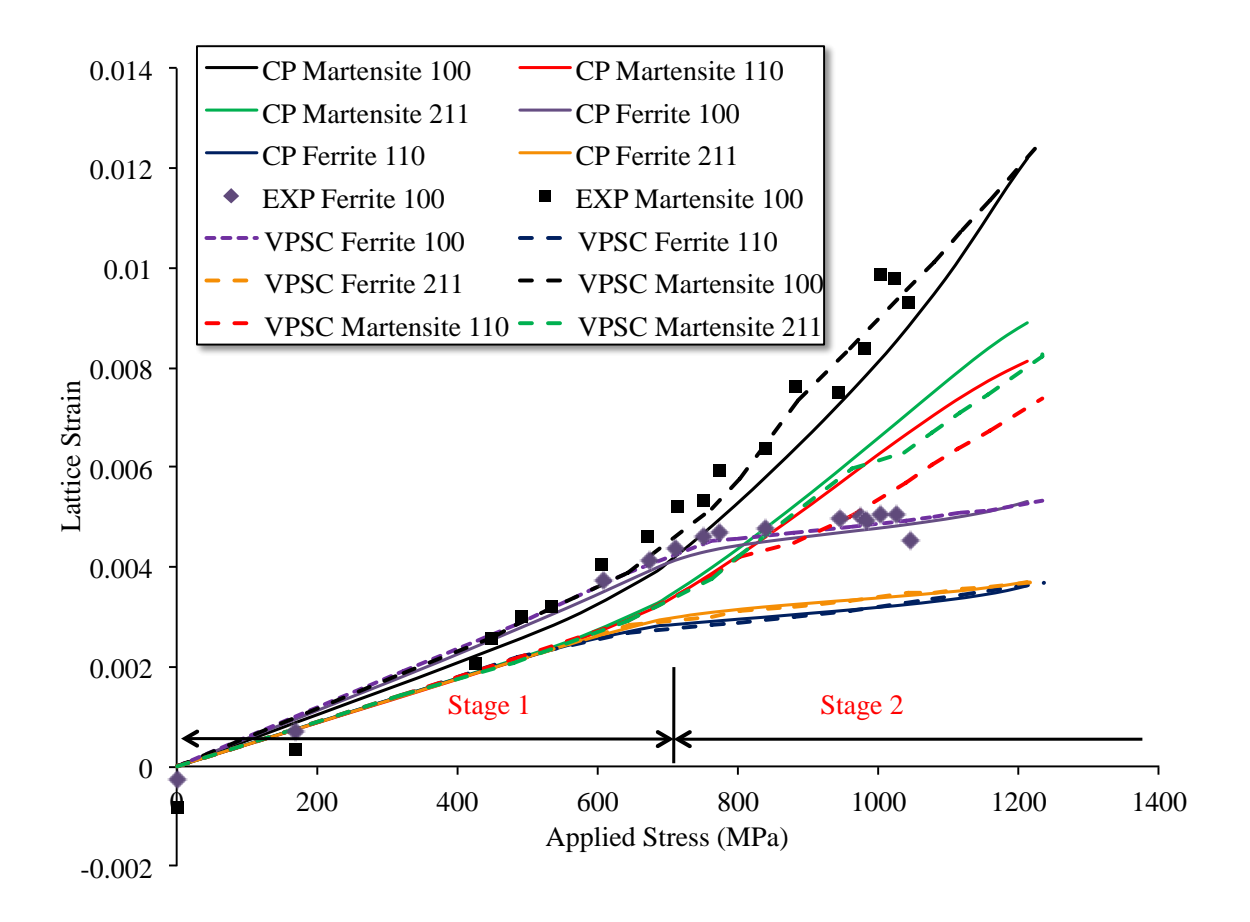


Figure 3

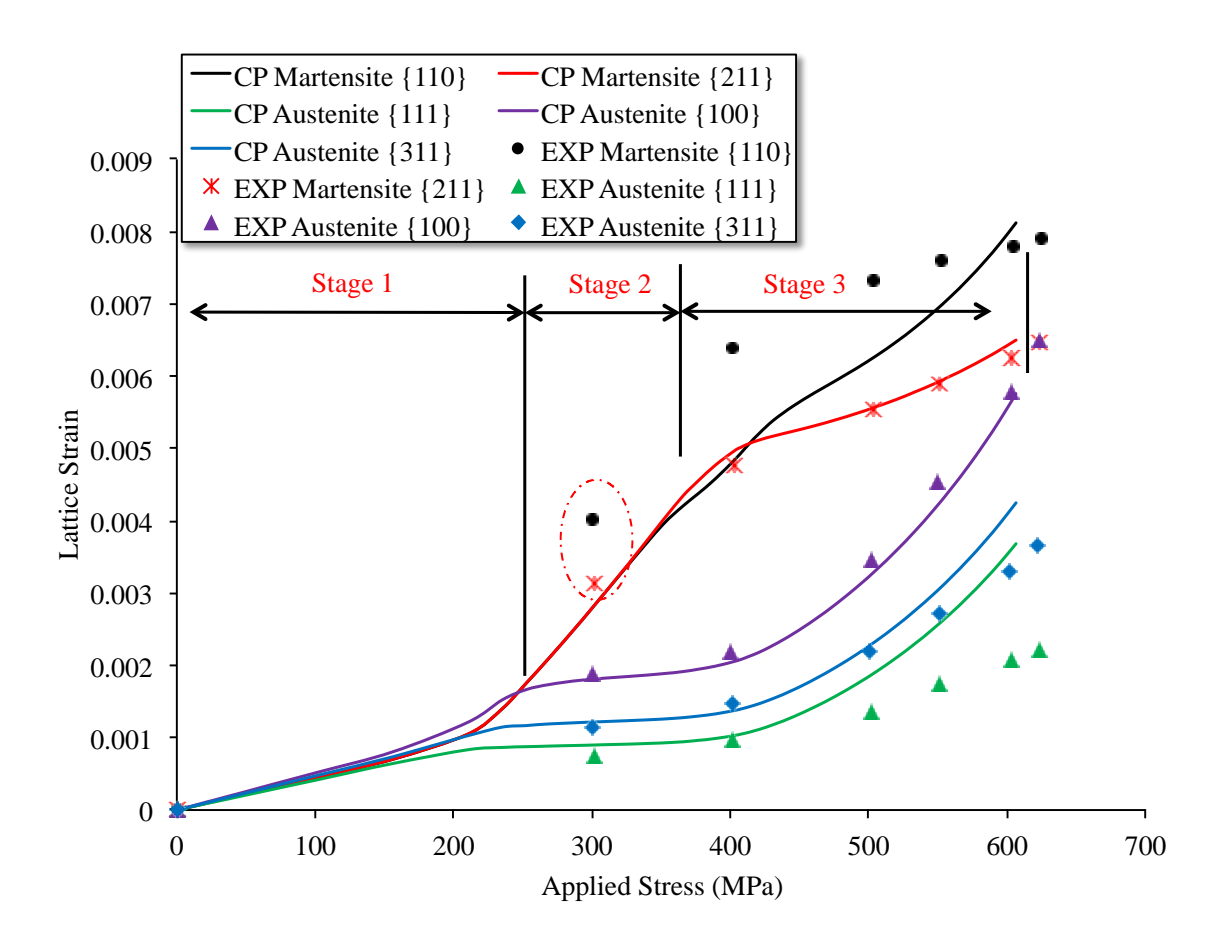


Figure 4

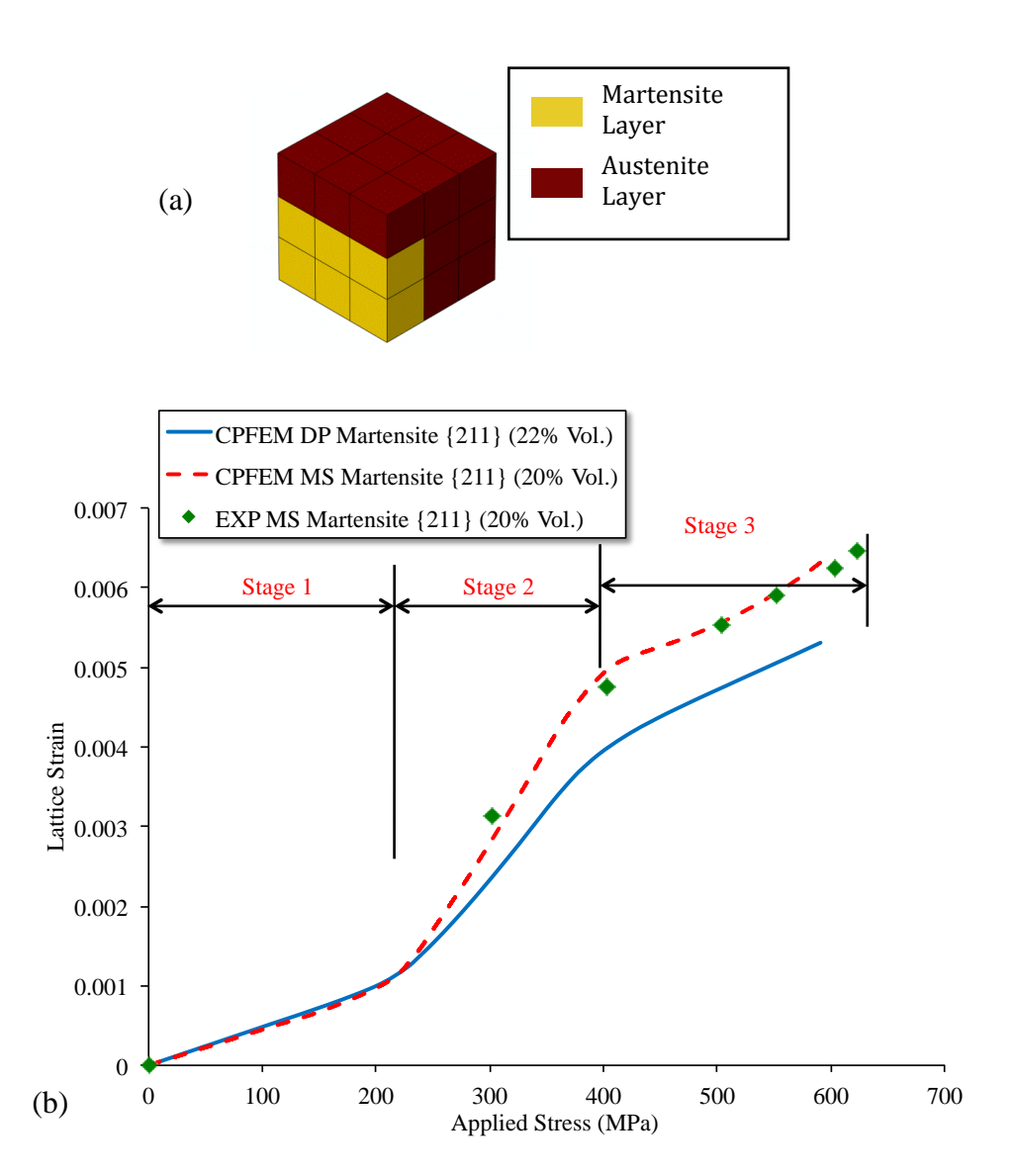


Figure 5